



# Unconventional sequence of correlated Chern insulators in magic-angle twisted bilayer graphene

Andrew T. Pierce<sup>1,5</sup>, Yonglong Xie<sup>0,1,2,5\infty</sup>, Jeong Min Park<sup>0,2,5</sup>, Eslam Khalaf<sup>0,1,5</sup>, Seung Hwan Lee<sup>1</sup>, Yuan Cao<sup>0,2</sup>, Daniel E. Parker<sup>1</sup>, Patrick R. Forrester<sup>0,1</sup>, Shaowen Chen<sup>1</sup>, Kenji Watanabe<sup>0,3</sup>, Takashi Taniguchi<sup>0,4</sup>, Ashvin Vishwanath<sup>1</sup>, Pablo Jarillo-Herrero<sup>0,2\infty</sup> and Amir Yacoby<sup>0,1\infty</sup>

The interplay between strong electron-electron interactions and band topology can produce electronic states that spontaneously break symmetries. The discovery of flat bands in magic-angle twisted bilayer graphene (MATBG)1-3 with non-trivial topology<sup>4-7</sup> has provided a compelling platform in which to search for new symmetry-broken phases. Recent scanning tunnelling microscopy8,9 and transport experiments<sup>10-13</sup> have revealed a sequence of topological insulating phases in MATBG near integer filling of the electronic bands produced by the moiré pattern. These correspond to a simple pattern of flavour-symmetry-breaking Chern insulators that fill bands of different flavours one after the other. Here we report the high-resolution local compressibility measurements of MATBG with a scanning single-electron transistor, which reveal an additional sequence of incompressible states with unexpected Chern numbers observed down to zero magnetic field. We find that the Chern numbers for eight of the observed incompressible states are incompatible with the simple picture in which the bands are sequentially filled. We show that the emergence of these unusual incompressible phases can be understood as a consequence of broken translation symmetry that doubles the moiré unit cell and splits each flavour band in two. Our findings expand the known phase diagram of MATBG, and shed light on the origin of the close competition between different correlated phases in the system.

Strongly interacting electrons in the flat bands of magic-angle twisted bilayer graphene (MATBG) give rise to a host of exotic correlated states including superconducting<sup>3,14,15</sup>, correlated insulating<sup>2,14,15</sup> and ferromagnetic phases<sup>15-18</sup>. This rich phase diagram is enabled by strong interactions<sup>19-22</sup> and the unique band structure of MATBG, which can be described as two fourfold degenerate sets of bands with opposite Chern numbers  $C = \pm 1$  (refs. <sup>7,23,24</sup>) if the  $C_2T$  symmetry that protects the Dirac points is broken<sup>25</sup>. To date, all Chern insulator (ChI) phases have been reported to result from successively filling these  $C=\pm 1$  bands. For example, hexagonal boron nitride (hBN) alignment breaks C2 symmetry and gaps the Dirac points to form a set of degenerate flat bands with opposite Chern numbers in opposite valleys. Interactions further lift this degeneracy, resulting in a valley-polarized ChI with C=1, consistent with experiment<sup>17</sup>. More recent studies<sup>8–13,26</sup> have shown that without the alignment of hBN to graphene, the combination of intrinsic electron-electron interactions and an applied perpendicular magnetic field is sufficient to isolate four degenerate bands with the same Chern number for both valleys and to drive the system into a series of flavour-polarized ChI phases. In both scenarios, the observed ChIs for positive or negative filling carry only positive or negative Chern numbers, respectively, and satisfy an even-odd symmetry where even or odd filling factors exhibit even or odd Chern numbers.

In this work, we report the discovery of additional incompressible states with unexpected Chern numbers in MATBG enabled by high-resolution, non-invasive local compressibility measurements using a scanning single-electron transistor (SET). At zero magnetic field, we detect and extract clear thermodynamic gaps at  $\nu = 0, +1$ , +2 and +3. Applying a modest perpendicular magnetic field allows us to unravel the complex topological character of these incompressible states and establish that several ChIs are stable even at zero magnetic field, despite close competition with nearly degenerate trivial insulators. We find a family of incompressible states originating from odd or even moiré band filling that carry even or odd Chern numbers, respectively, many of which are invisible in transport measurements on the same device. These states are difficult to reconcile with theories proposed so far in which the  $C=\pm 1$  bands are filled sequentially, and suggest that an unknown mechanism that reconstructs the topology of the bands is at work. We propose that the effect of the electron-electron interaction is to favour states that double the moiré unit cell, splitting each  $C = \pm 1$  band into one band with  $C=\pm 1$  and one with C=0, and that this simple mechanism is capable of describing the full sequence of the observed incompressible states. Our results constitute evidence for an additional class of interaction-driven ground states in MATBG, and demonstrate the critical role of symmetry breaking and topology in understanding the properties of the system.

The measurement protocol is schematically depicted in Fig. 1a and has been described elsewhere<sup>27</sup>. The hBN-encapsulated MATBG device (Fig. 1b) was fabricated using the 'tear-and-stack' technique (Methods). Global transport measurements at zero magnetic field (Fig. 1c; Fig. 1b shows the circuit) reveal strong thermally activated peaks in the four-terminal longitudinal resistance  $R_{xx}$  between the charge neutrality point (CNP) and full filling of the conduction moiré flat band. The pronounced activated behaviour of  $R_{xx}$ —particularly near the CNP—suggests the presence of a gap at the CNP (Extended Data Fig. 1), likely because of alignment between the graphene sheet and hBN substrate (Methods and Extended Data Fig. 2 provide additional evidence of alignment with hBN). Furthermore, we find a marked drop in resistance near  $n=-1.97\times10^{12}\,\mathrm{cm}^{-2}$ 

<sup>&</sup>lt;sup>1</sup>Department of Physics, Harvard University, Cambridge, MA, USA. <sup>2</sup>Department of Physics, Massachusetts Institute of Technology, Cambridge, MA, USA. <sup>3</sup>Research Center for Functional Materials, National Institute for Materials Science, Tsukuba, Japan. <sup>4</sup>International Center for Materials Nanoarchitectonics, National Institute for Materials Science, Tsukuba, Japan. <sup>5</sup>These authors contributed equally: Andrew T. Pierce, Yonglong Xie, Jeong Min Park, Eslam Khalaf. <sup>™</sup>e-mail: yxie1@g.harvard.edu; pjarillo@mit.edu; yacoby@g.harvard.edu

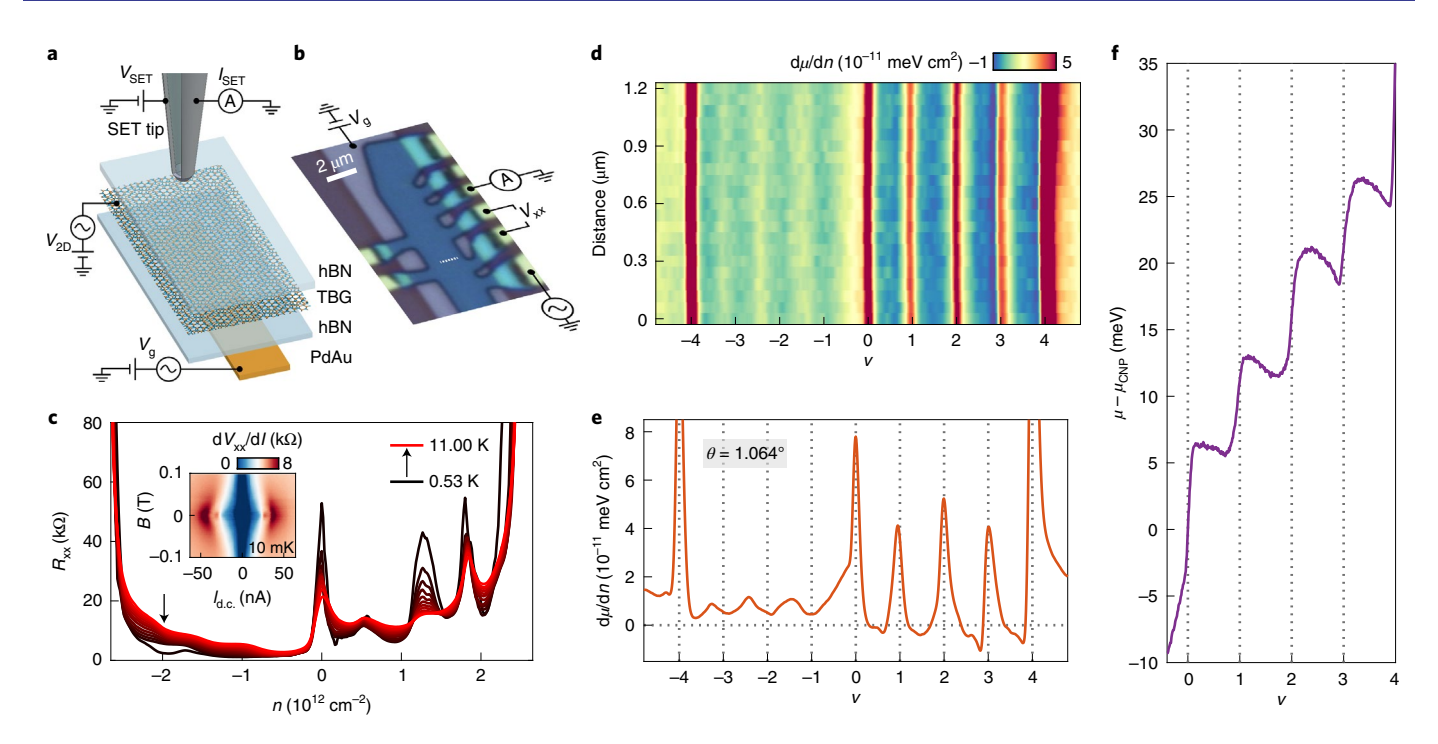
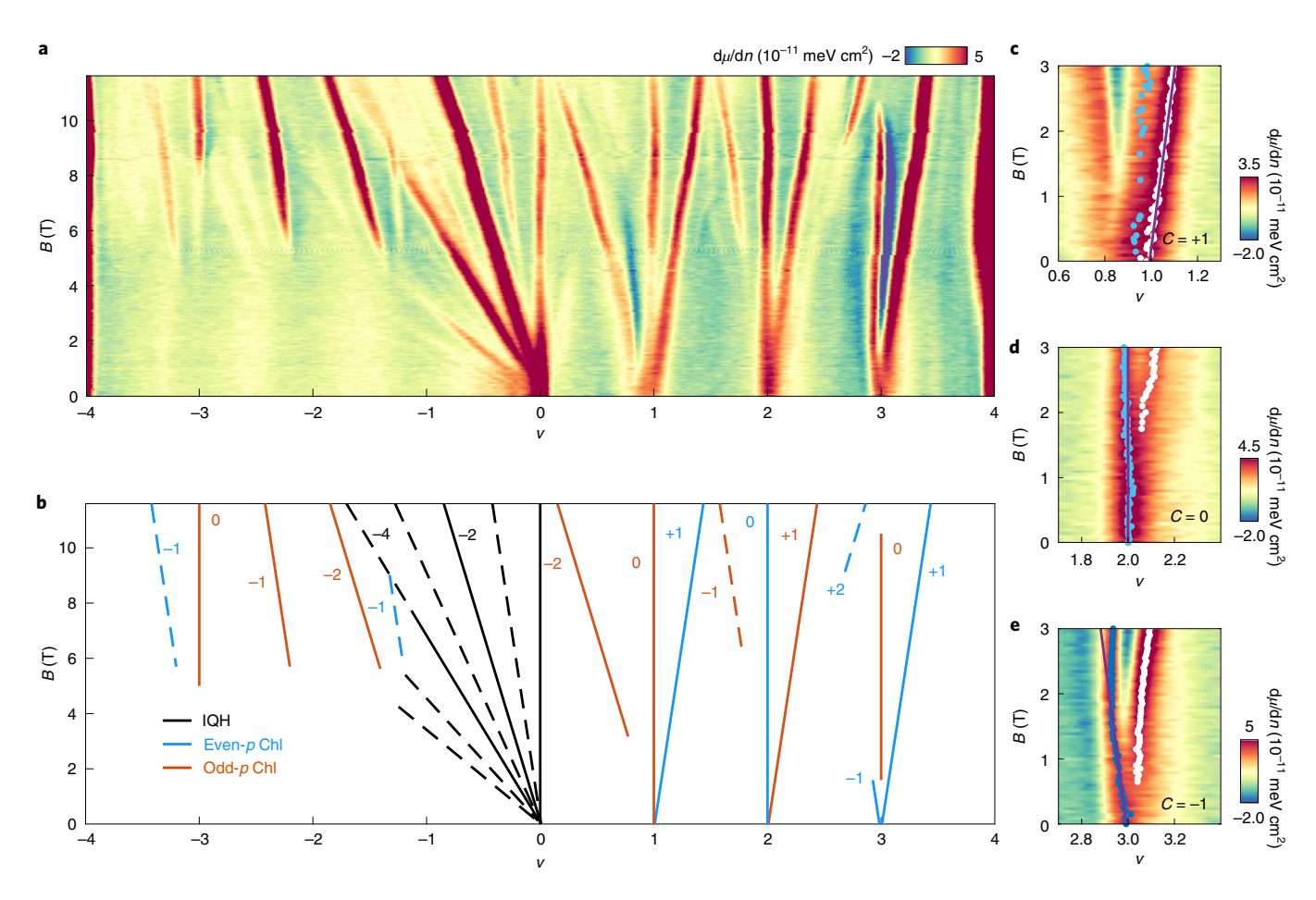


Fig. 1 | Thermodynamic gaps of correlated insulators in MATBG at zero magnetic field. a, Schematic of the scanning SET measurement setup.  $V_{\text{SET}}$  is the voltage bias applied across the SET.  $I_{\text{SET}}$  is the SET current.  $V_{\text{2D}}$  and  $V_{\text{g}}$  are voltages applied to twisted bilayer graphene (TBG) and the back gate, respectively. **b**, Optical image of the device and configuration used for transport measurement. The longitudinal voltage drop is denoted  $V_{\text{xx}}$ . **c**, Four-terminal longitudinal resistance  $R_{\text{xx}}$  as a function of carrier density measured at different temperatures ranging from 0.53 K (black trace) to 11.00 K (red trace) using the circuit shown in **b**. Inset: dilution refrigerator ( $T \approx 10 \text{ mK}$ ) measurement of the differential resistance as a function of the applied d.c. bias current  $I_{\text{dc}}$  and out-of-plane magnetic field B measured at density  $n = -1.97 \times 10^{12} \text{ cm}^{-2}$  (indicated by the arrow in the main plot). **d**, Local inverse compressibility  $d\mu/dn$  as a function of moiré band filling factor  $\nu$  measured along the white dashed line (1.2 μm) in **b**. **e**, Spatially averaged  $d\mu/dn$  obtained from **d**, showing incompressible peaks precisely aligned at  $\nu = 0$ , 1, 2 and 3. **f**, Spatially averaged chemical potential  $\mu$  relative to its value at the CNP, denoted  $\mu_{\text{CNP}}$ , as a function of moiré band filling factor  $\nu$ , showing steps at precisely  $\nu = 0$ , 1, 2 and 3. At these locations, we find the gaps  $\Delta_{\nu}$  at filling factors  $\nu = 0$ , 1, 2 and 3 to be  $\Delta_0 = 9 \text{ meV}$ ,  $\Delta_1 = 9 \text{ meV}$ ,  $\Delta_2 = 0 \text{ meV}$  and  $\Delta_3 = 0 \text{ meV}$ , respectively (Methods provides the gap extraction procedure).

(Extended Data Fig. 1), where separate transport measurements at 10 mK show that the resistance reaches zero. Finite resistance is restored by a modest magnetic field or bias current (Fig. 1c, inset), indicating the unusual emergence of superconductivity in MATBG aligned with hBN. Magnetotransport measurements further show that the magnetic field stabilizes ChIs, consistent with previous studies<sup>8-13</sup> (Extended Data Fig. 3). These measurements demonstrate that the device exhibits characteristic transport signatures of MATBG, which are compared with the compressibility measurements discussed below.

Turning to local compressibility, our first key observation is that the system exhibits clear thermodynamic gaps at v=0, +1, +2 and +3 at zero magnetic field. Figure 1d shows the inverse compressibility  $d\mu/dn$  measured along the white dotted line indicated in Fig. 1b. The absence of appreciable variation in the positions or intensities of the inverse compressibility features over 1.2 µm demonstrates that the region under study is highly homogeneous. The spatially averaged  $d\mu/dn$  (Fig. 1e) features two pronounced incompressible peaks at  $v = \pm 4$  associated with the energy gaps to the remote bands, the separation of which allows us to determine the local twist angle to be about 1.06° and to quantify the twist angle disorder to be no greater than 0.02° over a 2.6  $\mu m \! \times \! 1.2 \, \mu m$  region (Extended Data Fig. 4), highlighting the exceptional quality of the device. On the hole-doped side, we find a weak 'sawtooth' pattern, consistent with previous studies<sup>13,28,29</sup>, with peaks occurring approximately halfway between successive integer fillings. These peaks were interpreted as interaction-driven flavour symmetry breaking and similar features are expected to occur on the electron-doped side. Instead, we observe sharp incompressible peaks at precisely v = +1, +2 and +3, separated by regions of negative compressibility<sup>13,28,29</sup>, signalling the dominance of interactions and the formation of insulating states. Simultaneous direct current (d.c.) measurements of the chemical potential exhibit step-like changes and allow us to determine the energy gaps of these insulating states (Fig. 1f). We find the size of the gaps to be about 10 meV (Methods provides a comparison of the transport and tunnelling measurements), reaching as high as 13 meV at v = +2 (Extended Data Fig. 4). Importantly, we also observe a sharp, incompressible peak at the CNP with a corresponding gap of 9 meV, consistent with the expectation that the hBN substrate breaks the  $C_2T$  symmetry. The presence of a thermodynamic gap at the CNP, therefore, provides the prerequisite splitting of the conduction and valence flat bands for the emergence of insulating states with non-zero Chern numbers. These compressibility signatures, reproduced at many different locations (Extended Data Fig. 4), constitute the first unambiguous observation of the thermodynamic gaps of correlated insulating states in MATBG at zero magnetic field.

A topologically insulating gap can be classified according to its response to perpendicular magnetic fields, which encodes the Chern number of the corresponding incompressible state. Figure 2a shows inverse compressibility as a function of the moiré band filling factor  $\nu$  and perpendicular magnetic fields B up to 11.6 T. The data reveal a host of incompressible states that linearly disperse not only from the CNP but also from numerous integer fillings according to the Streda formula<sup>30</sup>  $dn/dB = C/\phi_0$ , where C is the Chern number and  $\phi_0$  is the magnetic flux quantum. Thus, we can identify the Chern number C associated with each incompressible state by extracting its slope on the n versus B plot (Fig. 2b), and characterize each state by its



**Fig. 2 | Unconventional sequence of Chls. a**, Local inverse compressibility  $d\mu/dn$  as a function of moiré band filling factor  $\nu$  measured between B=0 T and B=11.6 T. **b**, Schematic of the Wannier diagram corresponding to the observations in **a**. The strongest features are denoted by solid traces and weaker traces, by dashed lines. Integer quantum Hall (IQH) states emanating from the CNP are depicted in black, and Chls emanating from  $\nu=\pm 1,\pm 2$  and  $\pm 3$  are depicted in blue for even-p states and orange for odd-p states. **c-e**, Zoomed-in view of **a** around  $\nu=1$  (**c**),  $\nu=2$  (**d**) and  $\nu=3$  (**e**). Dark blue, light blue and white circles correspond to incompressible peak positions for C=-1, 0 and  $\pm 1$ , respectively. The solid lines in each panel mark the dominant ground state for each integer filling.

corresponding (C, s) value, where s is the moiré band filling. Near the CNP, we find a series of strong incompressible peaks (black lines, Fig. 2b) with  $C=-4, -2, 0, \ldots$ , which resemble energy gaps between the Landau levels originating from the Dirac point of the MATBG's band structure. However, we note that these states are also consistent with the selective filling of the  $C=\pm 1$  bands (Methods provides a detailed discussion).

Away from the CNP, the incompressible peaks at v = +1, +2 and +3 evolve strikingly as the magnetic field increases (Fig. 2c-e): the zero-field peaks rapidly split into multiple peaks. While features that do not follow a linear trajectory may stem from first-order phase transitions, here we focus on those that linearly disperse with the magnetic field. These features are associated with states with well-defined Chern numbers, many of which have not been reported so far. The observed incompressible states may be classified according to the parity p = C + s. The even-p states, such as (+1,+1), are generically expected in the presence of  $C_2$  symmetry breaking induced by hBN alignment. By contrast, the observed incompressible states with C = -2 and 0 from v = +1,  $C = \pm 1$  from v = +2, and C = 0 from v = +3 have odd p, and cannot be explained by simple flavour polarization in the presence of  $C_2T$  symmetry breaking, which only results in states with even p. Furthermore, scenarios involving mixing between the flat and remote bands<sup>31</sup> could, in principle, give rise to the C=0 insulators observed at  $\nu$  = 1 and 3, but this mechanism alone cannot produce both trivial and ChIs without invoking complex band mixing. The data, therefore, suggest that further reconstruction of the Chern bands takes place and leads to the observed sequence. Remarkably, tracking the peaks associated with the incompressible states near B = 0 T (Fig. 2c-e) reveals that the odd- and even-p states closely compete or coexist at a low field, leading to the insulating gaps observed at the zero field.

In contrast to the electron-doped side, the low-field compressibility on the hole-doped side displays conventional sawtooth patterns<sup>13,28,29</sup>, suggesting that the ratio of the interaction scale over the non-interacting bandwidth is smaller for holes than for electrons (Extended Data Fig. 5 and Methods). Under such conditions, a sufficiently large perpendicular magnetic field is expected to drive the system into flavour-polarized ChI states due to the strong orbital magnetic moments of the isolated Chern bands<sup>25,32</sup>, even if the ground state at zero field is metallic. When B reaches 5T, we begin to detect—in addition to Landau levels—prominent ChIs (Extended Data Fig. 6 and Methods provide a description of how they are distinguished) with C = -1 and 0 from  $\nu = -3$ , C = -1from  $\nu = -2$ , and C = -2 and -1 from  $\nu = -1$ , most of which have odd p and fall outside the sequence predicted by simple  $C_2T$  symmetry breaking. Crucially, the absence of odd-p states in transport (Extended Data Fig. 3) suggests that other devices exhibiting the

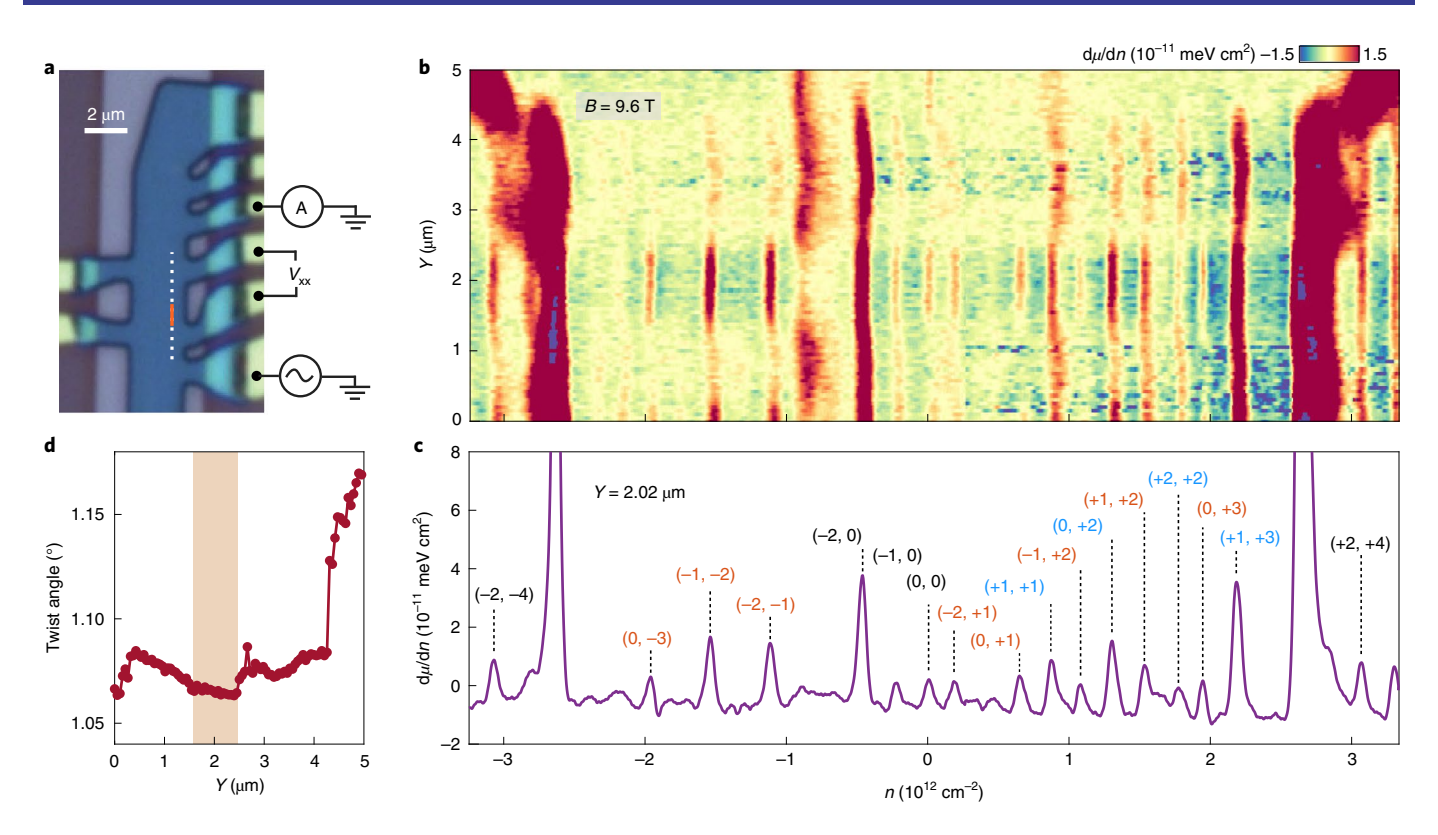


**Fig. 3** | **Robustness of even- and odd-**p **states against spatial inhomogeneity. a**, Optical image of the device and circuit configuration used for the transport measurements; the orange segment marks the region where the odd-p states are the strongest. **b**, Local inverse compressibility  $d\mu/dn$  as a function of density taken along the white dashed line in **a** at 9.6 T. **c**, Local inverse compressibility  $d\mu/dn$  at  $Y = 2.02 \, \mu m$  from **b**, where the incompressible peaks are labelled with the corresponding Chern number and moiré band filling. The blue and orange colours denote the even and odd parity states, respectively. **d**, Twist angle variation along the white dashed line in **a**. The shaded rectangle marks the regions where the odd-p states are the strongest.

conventional sequence in transport may exhibit a much richer set of incompressible states if studied using local compressibility.

Our ability to accurately determine the local twist angle at every position allows us to compare its relative influence on the evenand odd-p states. Figure 3b,c shows a measurement of  $d\mu/dn$  as a function of density over an extended spatial range of 5 µm, which includes the region over which the transport measurements are performed. While the odd-p states are robust and persist over approximately 1 µm (Fig. 3b and Extended Data Fig. 7), they disappear in some regions and are evidently more sensitive to spatial variation than the even-p states. By examining the local twist angle (Fig. 3d), we find that while the odd-*p* states are most robust in regions where the twist angle reaches the lowest observed value of about 1.06° and the twist angle is nearly constant, the very small variation in the twist angle observed over this region suggests that one or more different microscopic parameters other than the twist angle are controlling the appearance and disappearance of the odd-*p* states. These findings may explain the absence of odd-p states in transport measurements of the same device and in the literature. Overall, the odd-p states are reproducible and cannot be explained by the conventional picture of flavour polarization in MATBG and thus call for a re-examination of the topology and symmetry properties of the system.

The observation of robust odd-p states suggests that additional symmetry is broken, resulting in the reconstruction of Chern bands. Recent theoretical studies<sup>31,33</sup> have emphasized that away from the CNP, the charge density modulation in real space modifies the electronic band structure in momentum space considerably. This effect is reflected in the Hartree potential arising from the background electrons for positive  $\nu$  (Fig. 4a), where the inhomogeneous charge distribution raises the energies of the states at the K, K' and M points

with respect to those at the  $\Gamma$  point and favours populating electrons around the  $\Gamma$  point. As a result, a new possible ground state at  $\nu = +1$ emerges corresponding to a metal formed by half-filling two of the  $C = \pm 1$  bands, which competes with the single-valley-polarized ChI. Interactions can further lower the energy of the system by spontaneously breaking translation symmetry and folding the Brillouin zone in half<sup>34</sup>, which splits the band into two and forms an insulator (Fig. 4d). We emphasize that in this picture, translation symmetry is spontaneously broken solely as a result of electron-electron interactions, and not as a consequence of a sublattice potential induced by hBN. Because the Berry curvature is highly concentrated at the  $\Gamma$  point (Fig. 4b), the lower band (purple colour, Fig. 4d) inherits the Chern number of the original band  $(C=\pm 1)$ , while the Chern number of the upper band remains zero. On the hole-doped side, the Hartree potential acts with the opposite sign, raising the energies of the states at the  $\Gamma$  point and resulting in a lower band with C=0 and an upper band with  $C=\pm 1$ . Selectively filling these eight bands produces both even- and odd-p states for both electronand hole-doped sides observed in the experiment (Fig. 4e-j and Extended Data Fig. 8), suggesting that the odd-p states spontaneously break translation symmetry.

To further show that the odd-p states are energetically competitive, we perform calculations within a restricted self-consistent Hartree–Fock approximation (Supplementary Section II). For the odd-p case, we take a family of stripe states as trial wavefunctions, similar to those proposed in the recent density matrix renormalization group<sup>34,35</sup> and exact diagonalization<sup>36</sup> studies. These states fold the hexagonal moiré Brillouin zone into a rectangle, breaking not only translation symmetry but also  $C_3$  symmetry. Consistent with previous theoretical studies<sup>34–36</sup>, we find that the energy differences between odd- and even-p states at zero field are very sensitive to

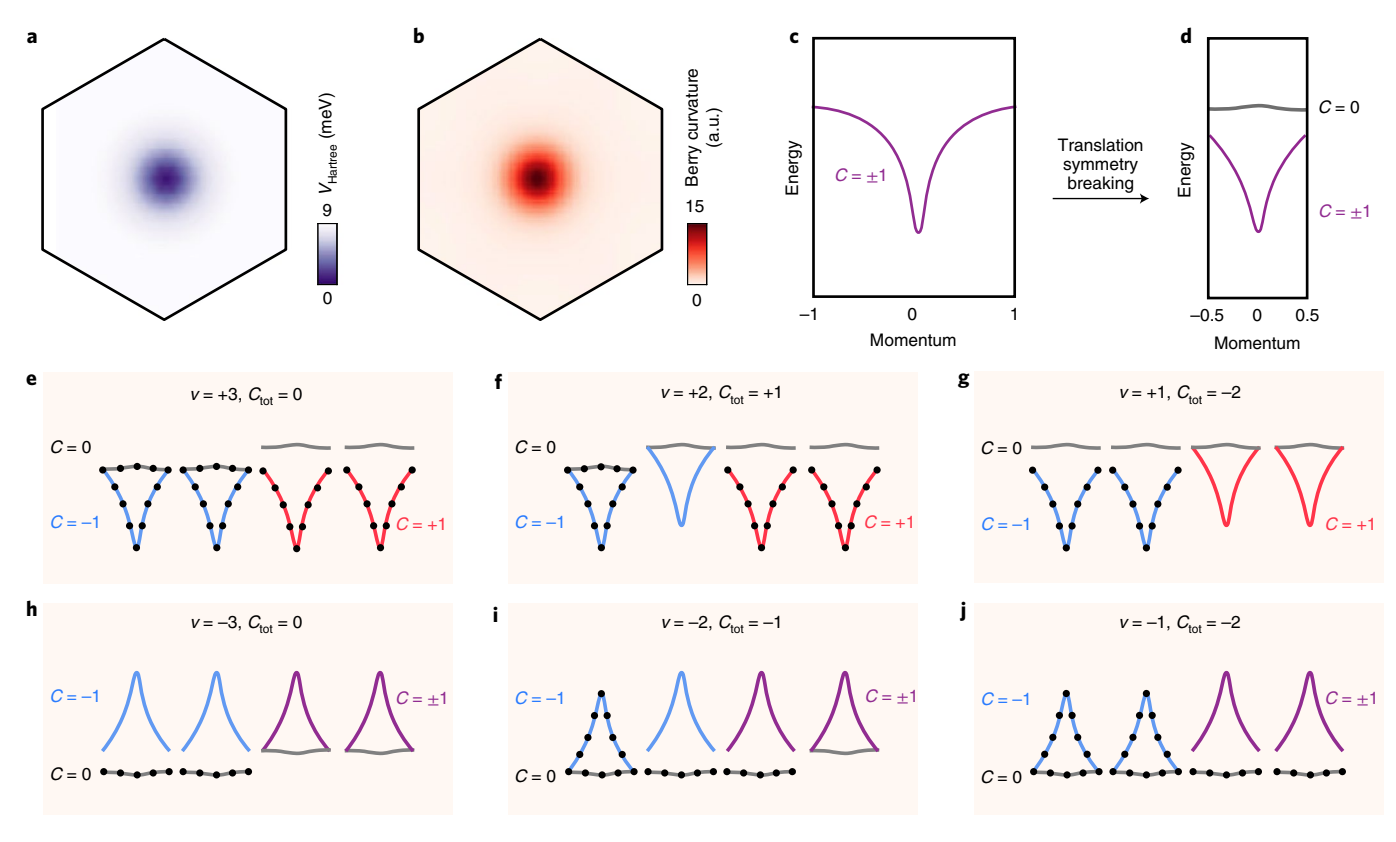


**Fig. 4 | Theoretical model with broken translational symmetry. a,b**, Hartree potential ( $V_{Hartree}$ ) (**a**) and Berry curvature (**b**) for the conduction flat bands within the first moiré Brillouin zone. The centre and corners of the hexagon correspond to the Γ and K (K') points, respectively. **c,d**, Sketch of the dispersion of conduction flat bands and their associated Chern numbers under the influence of the Hartree potential (**c**) and that with spontaneous translation symmetry breaking (**d**). **e-j**, Schematic of the band fillings (black circles indicate a filled band) that produce the representative translation symmetry-broken (odd-p) states with total Chern numbers  $C_{\text{tot}}$  experimentally observed for v = +3 (**e**), v = +2 (**f**), v = +1 (**g**), v = -3 (**h**), v = -2 (**i**) and v = -1 (**j**) (Extended Data Fig. 8 shows the full sequence). We note that only two C = -1 bands are necessary to produce the observed sequence on the hole-doped side.

the ratio  $w_0/w_1$ , where  $w_0$  is the interlayer tunnelling at the AA sites and  $w_1$  is that at the AB sites, and this energy difference can be as small as 0.5 meV per particle at  $\nu=3$  when  $w_0/w_1$  is large (Extended Data Fig. 9). Importantly, the results of our Hartree–Fock calculations are qualitatively independent of the strength of the sublattice potential, indicating that hBN alignment is not crucial in stabilizing the odd-p states.

Future studies will be required to determine whether hBN alignment and/or other microscopic parameters are essential ingredients for the occurrence of translation-symmetry-breaking states. More broadly, we anticipate translation symmetry breaking with incommensurate periodicity to occur and stabilize incompressible states at fractional moiré band filling, analogous to those recently reported in transition metal dichalcogenide moiré superlattices<sup>37,38</sup>, but stemming from Chern bands in this case. Importantly, our proposed mechanism isolates a key distinctive feature of the physics of MATBG: the interplay between the quantum geometry of wavefunctions—as manifested in the distribution of the Berry curvature—and strong electron-electron interactions. Finally, our finding of translation-symmetry-broken states down to zero magnetic field expands the rich phase diagram of MATBG, and their absence in transport highlights the power of local thermodynamic measurements for providing new insights into the competition between different phases in this strongly correlated electron system.

## Online content

Any methods, additional references, Nature Research reporting summaries, source data, extended data, supplementary infor-

mation, acknowledgements, peer review information; details of author contributions and competing interests; and statements of data and code availability are available at https://doi.org/10.1038/s41567-021-01347-4.

Received: 29 December 2020; Accepted: 5 August 2021; Published online: 30 September 2021

#### References

- Bistritzer, R. & MacDonald, A. H. Moiré bands in twisted double-layer graphene. Proc. Natl Acad. Sci. USA 108, 12233–12237 (2011).
- Cao, Y. et al. Correlated insulator behaviour at half-filling in magic-angle graphene superlattices. *Nature* 556, 80–84 (2018).
- Cao, Y. et al. Unconventional superconductivity in magic-angle graphene superlattices. *Nature* 556, 43–50 (2018).
- Po, H. C., Zou, L., Vishwanath, A. & Senthil, T. Origin of Mott insulating behavior and superconductivity in twisted bilayer graphene. *Phys. Rev. X* 8, 031089 (2018).
- Song, Z. et al. All magic angles in twisted bilayer graphene are topological. Phys. Rev. Lett. 123, 036401 (2019).
- Ahn, J., Park, S. & Yang, B.-J. Failure of Nielsen-Ninomiya theorem and fragile topology in two-dimensional systems with space-time inversion symmetry: application to twisted bilayer graphene at magic angle. *Phys. Rev.* X 9, 021013 (2019).
- Po, H. C., Zou, L., Senthil, T. & Vishwanath, A. Faithful tight-binding models and fragile topology of magic-angle bilayer graphene. *Phys. Rev. B* 99, 195455 (2019).
- Nuckolls, K. P. et al. Strongly correlated Chern insulators in magic-angle twisted bilayer graphene. *Nature* 588, 610–615 (2020).
- Choi, Y. et al. Correlation-driven topological phases in magic-angle twisted bilayer graphene. *Nature* 589, 536–541 (2021).

- Wu, S., Zhang, Z., Watanabe, K., Taniguchi, T. & Andrei, E. Y. Chern insulators, Van Hove singularities and topological flat bands in magic-angle twisted bilayer graphene. *Nat. Mater.* 20, 488–494 (2021).
- Saito, Y. et al. Hofstadter subband ferromagnetism and symmetry-broken Chern insulators in twisted bilayer graphene. Nat. Phys. 17, 478–481 (2021).
- Das, I. et al. Symmetry-broken Chern insulators and Rashba-like Landau-level crossings in magic-angle bilayer graphene. Nat. Phys. 17, 710–714 (2021).
- Park, J. M., Cao, Y., Watanabe, K., Taniguchi, T. & Jarillo-Herrero, P. Flavour Hund's coupling, Chern gaps and charge diffusivity in moiré graphene. Nature 592, 43–48 (2021).
- Yankowitz, M. et al. Tuning superconductivity in twisted bilayer graphene. Science 363, 1059–1064 (2019).
- 15. Lu, X. et al. Superconductors, orbital magnets and correlated states in magic-angle bilayer graphene. *Nature* **574**, 653–657 (2019).
- Sharpe, A. L. et al. Emergent ferromagnetism near three-quarters filling in twisted bilayer graphene. Science 365, 605–608 (2019).
- Serlin, M. et al. Intrinsic quantized anomalous Hall effect in a moiré heterostructure. Science 367, 900–903 (2020).
- 18. Stepanov, P. et al. Untying the insulating and superconducting orders in magic-angle graphene. *Nature* **583**, 375–378 (2020).
- Xie, Y. et al. Spectroscopic signatures of many-body correlations in magic-angle twisted bilayer graphene. *Nature* 572, 101–105 (2019).
- Kerelsky, A. et al. Maximized electron interactions at the magic angle in twisted bilayer graphene. *Nature* 572, 95–100 (2019).
- Choi, Y. et al. Electronic correlations in twisted bilayer graphene near the magic angle. *Nat. Phys.* 15, 1174–1180 (2019).
- Jiang, Y. et al. Charge order and broken rotational symmetry in magic-angle twisted bilayer graphene. *Nature* 573, 91–95 (2019).
- Liu, J., Liu, J. & Dai, X. Pseudo Landau level representation of twisted bilayer graphene: band topology and implications on the correlated insulating phase. *Phys. Rev. B* 99, 155415 (2019).
- Bultinck, N. et al. Ground state and hidden symmetry of magic-angle graphene at even integer filling. Phys. Rev. X 10, 031034 (2020).
- Bultinck, N., Chatterjee, S. & Zaletel, M. P. Mechanism for anomalous Hall ferromagnetism in twisted bilayer graphene. *Phys. Rev. Lett.* 124, 166601 (2020).

- Tomarken, S. L. et al. Electronic compressibility of magic-angle graphene superlattices. *Phys. Rev. Lett.* 123, 046601 (2019).
- Martin, J., Feldman, B. E., Weitz, R. T., Allen, M. T. & Yacoby, A. Local compressibility measurements of correlated states in suspended bilayer graphene. *Phys. Rev. Lett.* 105, 256806 (2010).
- Wong, D. et al. Cascade of electronic transitions in magic-angle twisted bilayer graphene. Nature 582, 198–202 (2020).
- Zondiner, U. et al. Cascade of phase transitions and Dirac revivals in magic-angle graphene. *Nature* 582, 203–208 (2020).
- Streda, P. Theory of quantised Hall conductivity in two dimensions. J. Phys. C 15, L717–L721 (1982).
- 31. Xie, M. & MacDonald, A. H. Nature of the correlated insulator states in twisted bilayer graphene. *Phys. Rev. Lett.* **124**, 097601 (2020).
- Liu, J., Ma, Z., Gao, J. & Dai, X. Quantum valley Hall effect, orbital magnetism, and anomalous Hall effect in twisted multilayer graphene systems. *Phys. Rev. X* 9, 031021 (2019).
- Guinea, F. & Walet, N. R. Electrostatic effects, band distortions, and superconductivity in twisted graphene bilayers. *Proc. Natl Acad. Sci. USA* 115, 13174–13179 (2018).
- Kang, J. & Vafek, O. Non-Abelian Dirac node braiding and near-degeneracy of correlated phases at odd integer filling in magic-angle twisted bilayer graphene. *Phys. Rev. B* 102, 035161 (2020).
- Chen, B.-B. et al. Realization of topological Mott insulator in a twisted bilayer graphene lattice model. Preprint at https://arxiv.org/abs/2011.07602 (2020).
- Xie, F. et al. Twisted bilayer graphene. VI. An exact diagonalization study at nonzero integer filling. *Phys. Rev. B* 103, 205416 (2021).
- Regan, E. C. et al. Mott and generalized Wigner crystal states in WSe<sub>2</sub>/WS<sub>2</sub> moiré superlattices. *Nature* 579, 359–363 (2020).
- 38. Xu, Y. et al. Correlated insulating states at fractional fillings of moiré superlattices. *Nature* 587, 214–218 (2020).

**Publisher's note** Springer Nature remains neutral with regard to jurisdictional claims in published maps and institutional affiliations.

© The Author(s), under exclusive licence to Springer Nature Limited 2021

## Methods

Sample preparation. The MATBG device used in this study was fabricated using the standard 'tear-and-stack' technique<sup>39,40</sup>. Monolayer graphene and hBN flakes were first exfoliated on SiO<sub>2</sub>/Si substrates and subsequently analysed with optical microscopy and atomic force microscopy to determine their thickness and ensure their high quality. We used a poly(bisphenol A carbonate)/polydimethylsiloxane stamp on a glass slide to first pick up a 30-nm-thick hBN flake at 90 °C, which was then used to tear and pick up half the graphene flake at room temperature. The Si substrate was then rotated by 1.1°, and the remaining flake was picked up at room temperature. The resulting stack was then released on the pre-stacked 45 nm hBN/PdAu back gate at 175 °C. The device geometry was defined by electron-beam lithography and reactive ion etching. Cr/Au electrical contacts to MATBG were made by the standard edge-contact method.

**Transport measurements.** Temperature-dependent transport measurements were performed in a  $^3$ He cryostat with a base temperature of approximately 500 mK, by applying current to a resistive heater located on the  $^3$ He plate. Magnetotransport measurements were performed in a Leiden dilution fridge refrigerator, with a nominal base temperature of 10 mK. Standard low-frequency lock-in techniques were used to measure the resistance with an excitation current of approximately 1 nA at a frequency of 17.777 Hz.

Compressibility measurements. All the compressibility measurements were made in the same <sup>3</sup>He cryostat used for the temperature-dependent transport measurements. The SET tips were fabricated using a procedure described elsewhere<sup>27</sup>. The SET tip had a diameter of approximately 100 nm, and was held approximately 100 nm above the encapsulated MATBG. Compressibility measurements were performed using d.c. and alternating current (a.c.) protocols similar to those described in ref. 27. The SET is sensitive to changes in the local electrostatic potential  $\phi$ , which is related to the chemical potential  $\mu$  of MATBG by  $\delta\mu = -e\delta\Phi$  when the system is in equilibrium. In the a.c. scheme, an a.c. voltage is applied to the PdAu back gate to weakly modulate the carrier density of the MATBG, and the corresponding a.c. SET current is normalized by the signal produced by a small a.c. bias simultaneously applied to the sample and gate to obtain the inverse compressibility  $d\mu/dn$ . To hold the response of the SET fixed, an analogue proportional-integral-derivative controller is used to maintain the d.c. SET current at a fixed value by controlling the d.c. voltage of the sample and back gate relative to the tip. The corresponding change in d.c. voltage provides a direct measure of  $\mu(n)$ .

Correction for direct gating and extraction of gaps from  $\mu(n)$  data. When the SET tip is held at a finite height, the direct gating of the SET by the back gate introduces a constant offset to the measured compressibility. This contribution can be mitigated by subtracting a small experimentally determined constant calculated from a reference measurement near the middle of the sample and very close to the surface. This correction corresponds to subtracting a linear background from  $\mu(n)$ . Gaps are estimated from  $\mu(n)$  by linearly extrapolating back to integer  $\nu$ , which is invariant in the presence of a linear background.

Superlattice density and twist angle determination. To determine the superlattice density, we first calibrate the capacitance between the back gate and MATBG using the slope of the Landau fan near the CNP (Fig. 2a). Superlattice density  $n_s$  is estimated from the product of the capacitance and the back-gate voltage difference between the incompressible peaks associated with the full-filling gaps in compressibility measurements. The estimate of superlattice density is confirmed by examining the Landau fans outside the fully filled flat bands (black lines, Extended Data Fig. 2c). Local twist angle  $\theta$  is calculated using the relation  $n_s \approx 8\theta^2/\sqrt{3}a^2$ , where  $a=0.246\,\mathrm{nm}$ —the lattice constant of graphene. The accuracy of the twist angle estimate is determined by the increment in the back-gate sweep. We can conveniently achieve 0.1% precision in determining the superlattice density, which corresponds to a relative accuracy of 0.001°. The conversion from back-gate voltage to moiré band filling factor  $\nu$  is a linear transformation and the electron (hole) full-filling voltage corresponds to  $\nu=+4$  (-4), respectively.

Evidence for hBN alignment. Extended Data Fig. 2a shows the optical image of the stack before etching. The crystallographic edges of the graphene sheet and the bottom hBN are aligned with a  $60^\circ$  angular offset, suggesting possible alignment between graphene and hBN. This is confirmed by the observation of an additional set of Landau fans in the local compressibility measurement that intersect the density axis at a different value than those of MATBG (orange lines, Extended Data Fig. 2c), which corresponds to a misalignment of  $0.36\pm0.02^\circ$  between graphene and hBN. We emphasize that the local nature of our measurement rules out the possibility of this additional moiré subband feature arising from inhomogeneity in twist angle between the graphene sheets. Taken together, these features are consistent with the observation of a thermodynamic gap at the CNP in both thermal activation and local compressibility measurements and they constitute strong evidence for alignment between MATBG and hBN.

**Twist angle variation and its influence on thermodynamic gaps.** As described in the main text, our local compressibility measurements allow us to determine

the local twist angle and we find that the peak-to-peak variation of the twist angle over a  $2.6\,\mu m \times 1.2\,\mu m$  region is around  $0.02^\circ$  with a standard deviation of  $0.0046^\circ$ . We find that the thermodynamic gaps at  $\nu=0,+1,+2$  and +3 are present over the whole region (Extended Data Fig. 4d–g), demonstrating the robustness of our findings. Moreover, we find that the strength of the gaps at  $\nu=+1,+2$  and +3 is very sensitive to local changes that could include twist angle variation and strain and lattice relaxation, whereas the gap at the CNP remains nearly unchanged.

Comparison of gap values to those obtained from transport and tunnelling experiments. The energy gap of the zero-field ChIs found by us is about 10 meV, which is more than 30 times the activation gap extracted from the transport experiments (Extended Data Fig. 1). In addition, the size of the insulating gap extracted by us is at least a few millielectronvolts larger than those observed in tunnelling spectroscopy measurements <sup>19-21</sup>. We emphasize that our technique does not suffer from the possible soft Coulomb gap<sup>41</sup>, which complicates the interpretation of apparent gaps in the tunnelling spectra, and that the tip–sample distance in our setup is approximately 100 nm compared with a few angstroms, allowing us to avoid possible tip-induced screening effects that recent transport studies <sup>18,42</sup> suggest may play an important role in tunnelling experiments.

Discussion of the possible origin of incompressible states near the CNP. Near the CNP, we find a sequence of strong incompressible states with  $C=-4, -2, 0, \dots$ which may be associated with Landau levels but may also arise due to selective filling of the  $C=\pm 1$  bands. We discuss these two possibilities in detail below. In the Landau level picture, an eightfold degeneracy is expected due to spin, valley and layer degrees of freedom in the absence of any symmetry breaking. Heterostrain that is present in our device breaks the C3 symmetry (Extended Data Fig. 4c) and reduces the degeneracy to four. The observation of a strong C = -2 state likely results from  $C_2$  symmetry breaking, as suggested by a recent theoretical study43. Finally, the absence of incompressible peaks on the electron-doped side of the CNP reflects a strong intrinsic electron-hole asymmetry, which is also evident in our transport and compressibility measurements at zero magnetic field. In particular, the sharp onset of the CNP peak on the electron-doped side suggests a large effective mass, disfavouring the formation of Landau levels. On the other hand, in the picture of selectively filled  $C = \pm 1$  bands, the presence of a strong sublattice potential induced by hBN alignment gives rise to two fourfold degenerate flat bands above and below the CNP, each with a total Chern number of zero. Thus, we conclude that only C=0 can occur near the CNP, as seen on the electron-doped side. The observation of strong C = -4 and -2 states then suggests that the sublattice potential is weaker for holes than electrons, possibly due to only one graphene sheet being aligned with hBN, and hence, the states may result from selectively filling the  $C = \pm 1$  bands. We note that the effect of hBN is not required to capture the odd-p states observed on the hole-doped side as only two C = -1bands are necessary to produce the observed sequence.

**Mean-field simulation of inverse compressibility.** To understand the electronhole asymmetry in the measured inverse compressibility at zero magnetic field, we performed a mean-field calculation to simulate the inverse compressibility of the system as a function of the filling factor, similar to that described in ref. <sup>13</sup>. We consider the total free energy of the system G as a function of the total filling  $\nu$ , which is the sum of the fillings of the four flavours  $\nu_r$ . Each flavour has its own chemical potential  $\mu_P$  which is related to  $\nu_i$  by  $\nu_i = \int\limits_{\mu_I}^{\mu_I} D\left(\varepsilon\right) \, d\varepsilon$ , where  $D(\varepsilon)$  is the single-particle density of states. The free energy consists of a kinetic term

$$G_{k}=\sum_{i}\int\limits_{0}^{\mu_{i}}\epsilon D\left(\epsilon\right)\mathrm{d}\epsilon$$
 and a Coulomb term  $G_{U}=U\sum_{i\neq j}v_{i}v_{j}-J\sum_{i}v_{i}^{2}$ , where  $U$  and

J represent the strength of the Coulomb repulsion and exchange interaction in an extended Hubbard model within the mean-field approximation, respectively. We note that the effective total Coulomb interaction is given by  $U_{\text{tot}} = U + 2J$ . The inverse compressibility of the system is calculated from the relation  $\frac{\partial \mu}{\partial n} = \frac{\partial^2 G}{\partial n^2}$ . To capture the essential physics of the system, we approximate the density of states of MATBG by a triangular function, where each flat band has a bandwidth of W. Our calculations (Extended Data Fig. 5) show that the inverse compressibility of the system exhibits three distinct behaviours depending on the  $U_{tot}/W$  ratio. When  $U_{tot}/W$  is small, the effect of interactions on the inverse compressibility is negligible. When  $U_{tot}/W$  is greater than a critical value  $\alpha$  but smaller than a second critical value  $\beta$ , the system undergoes a cascade of phase transitions, as previously reported<sup>13,</sup> When  $U_{tot}/W$  further exceeds  $\beta$ , gaps start to develop at integer fillings. Extended Data Fig. 5f shows that by accounting for the difference in bandwidth between the conduction and valence flat bands, including an asymmetric sublattice gap at the CNP (as shown in Fig. 1f), our calculation captures all the salient features observed in the experiment. Moreover, calculations with and without a gap at the CNP using the same interaction strength reveal that the presence of a gap at the CNP increases the gap size at integer fillings. However, interactions are key in driving the formation of gaps at integer fillings, as shown in Extended Data Fig. 5g.

**ChIs versus Landau levels.** Here we summarize the key arguments that allow us to identify the insulating states observed in our experiment as ChIs. First, Landau quantization alone cannot explain the persistence of incompressible states at

 $\nu=1,2$  and 3 down to very low or zero magnetic field. Second, the magnitude of the incompressible peaks associated with ChIs is substantially larger than the Landau levels emanating from integer fillings. This is shown in Extended Data Fig. 6, which shows much smaller peaks for the Landau level states (such as (C,s)=(-3,-2) and (-4,-1)) compared with those identified as ChIs (for example, (-1,-2) and (-2,-1)). Moreover, the energy gaps associated with these two classes of states differ substantially (Extended Data Fig. 6b), indicating that they are governed by different energy scales. Finally, if the observed states with a non-zero Chern number arise from a simple Landau quantization, there would be neither a reason for the conspicuous absence of (-1,+1) nor the expectation of the particular sequence (C=0,-1 and -2 for  $\nu=-3,-2$  and -1, respectively), which contradicts with the expected degeneracy for Landau levels.

**Hartree potential.** To examine the influence of Hartree potential on the system, we consider the interaction projected onto the eight flat bands labelled by spin, valley and band indices. The Hartree Hamiltonian can be written in terms of the density matrix  $P_{\alpha,\beta} = <\hat{c}_{\alpha,\mathbf{k}}^\dagger\hat{c}_{\beta,\mathbf{k}}^\dagger$  and the form factor matrix  $[\Lambda_{\mathbf{q}}(\mathbf{k})]_{\alpha,\beta} = <u_{\alpha,\mathbf{k}}|u_{\beta,\mathbf{k}+\mathbf{q}}\rangle$ , where  $\alpha$  and  $\beta$  are the combined indices for the sublattice, valley and spin labelling of the states within the flat bands, and  $|u_{\alpha,\mathbf{k}}\rangle$  denote single-particle wavefunctions. The Hartree Hamiltonian is given by

$$\mathcal{H}_{\mathrm{H}}\left(\mathbf{k}\right) = \frac{1}{A} \sum_{\mathbf{G}} V_{\mathbf{G}} \Lambda_{\mathbf{G}}\left(\mathbf{k}\right) M_{\mathbf{G}}, \qquad M_{\mathbf{G}} = \sum_{\mathbf{k}' \in \mathrm{BZ}} \mathrm{tr} \Lambda_{-\mathbf{G}}\left(\mathbf{k}'\right) \left(2P\left(\mathbf{k}'\right) - 1\right),$$

where **G** is a reciprocal lattice vector in the Brillouin zone (BZ) and *P* is a projector whose eigenvalues are 0 and 1 for empty and fully filled bands, respectively. Because a fully filled (empty) band labelled by the index  $\alpha$  corresponds to  $P_{\alpha,\beta} = \delta_{\alpha,\beta} \left(P_{\alpha,\beta} = 0\right)$ , respectively, the contribution of a fully filled (empty) band to  $M_G$  is  $\sum_{\mathbf{k}' \in \mathrm{BZ}} \left[ \Lambda_{-\mathbf{G}} \left( \mathbf{k}' \right) \right]_{\alpha,\alpha}$ . It can be numerically verified that this contribution is independent of  $\alpha$  to a very good approximation and thus can be identified with  $\frac{1}{8} \sum_{\mathbf{k}' \in \mathrm{BZ}} \mathrm{tr} \Lambda_{-\mathbf{G}} \left( \mathbf{k}' \right)$ . Hence, the Hartree potential due to a fully filled/empty band is given by  $V_{\mathrm{H}}(\mathbf{k})$  as follows.

$$V_{\mathrm{H}}\left(\mathbf{k}\right) = \pm \frac{1}{8A} \sum_{\mathbf{G}} V_{\mathbf{G}} \Lambda_{\mathbf{G}}(\mathbf{k}) \sum_{\mathbf{k}' \in \mathrm{BZ}} \mathrm{tr}(\Lambda_{-\mathbf{G}}\left(\mathbf{k}'\right))$$

This function is plotted in Fig. 4a, which exhibits a prominent dip centred at the  $\Gamma$  point. Consequently, once we fill n bands relative to the CNP (positive (negative) n corresponds to electron (hole) filling), the new electrons to be added to the system experience a dispersion modified by the addition of  $nV_{\rm H}(\mathbf{k})$ .

**Berry curvature.** To identify the topological character of the flat bands under the influence of Hartree potential, we compute the distribution of the Berry curvature. The alignment of the hBN substrate introduces a sublattice potential favouring one sublattice over the other. As a result, the Dirac cones at K and K' are gapped and we can simply label the states in each spin s and valley  $\tau=\pm K/K'$  sector by a band index  $\rho=\pm$ . In general, the Berry connection is a matrix in the band space, but here we are only interested in its diagonal part expressed as follows.

$$\mathbf{A}_{\alpha}(\mathbf{k}) = -i < u_{\alpha,\mathbf{k}} | \nabla_{\mathbf{k}} | u_{\alpha,\mathbf{k}} >$$

Here,  $\nabla_{\bf k}$  denotes the gradient with respect to  ${\bf k}.$  The gauge-invariant Berry curvature is

$$\Omega_{\alpha}(\mathbf{k}) = \partial_{k_{x}} A_{\alpha,y}(\mathbf{k}) - \partial_{k_{y}} A_{\alpha,x}(\mathbf{k})$$

and its momentum space integral yields the Chern number. Using the different symmetries, we can show that the Berry curvatures of the eight flat bands are related (Supplementary Section I). Therefore, it is sufficient to compute it for only one of the bands. The Berry curvature of the lower band in valley K is shown in Fig. 4b, whose weight is highly concentrated at the  $\Gamma$  point.

Dominance of odd-p states on the hole-doped side. Our Hartree–Fock calculations reveal that enhancements in bandwidth, such as that from the Hartree potential, increase the energy gain associated with forming the translation-symmetry-breaking states, suggesting an explanation for the dominance of odd-p states on the hole-doped side of the CNP. We find that the gap to the valence remote band is less than 18 meV, approximately 60% of that to the conduction remote band (Extended Data Fig. 10), and substantially smaller than the interaction energy of about 23 meV extracted from recent spectroscopic measurements<sup>19,28</sup>. Because the Hartree correction to the bandwidth becomes non-negligible when the gap separating the flat bands from the remote bands is smaller than the interaction strength, we expect considerable enhancement in the bandwidth of the valence flat band, favouring the translation-symmetry-breaking states on the hole-doped side.

**Possible role of magnetization.** Most of the salient features of our compressibility measurements can be captured within a phenomenological model of the free

energy of the system in which the magnetization and energy of each ChI band are taken as free fit parameters (Supplementary Section III). This toy model highlights the importance of including the effect of finite magnetization, without which only a single ChI emanating from each  $\nu$  is predicted to occur at a given magnetic field\*. However, states with C<0 on the electron-doped side are not captured within this phenomenological model. Because hBN alignment breaks the sublattice symmetry and generates bands with opposite Chern numbers at opposite valleys, the hBN alignment favours Chern bands with negative Chern numbers on the electron-doped side, regardless of spontaneous translation symmetry breaking. In addition, we speculate that the cascade of phase transitions may introduce corrections to the free energy of the C<0 states beyond the terms considered in our model.

## Data availability

Source data are provided with this paper. All other data that support the findings of this paper are available from the corresponding authors upon request.

## Code availability

The code that supports the findings of this study is available from the corresponding authors upon reasonable request.

#### References

- Cao, Y. et al. Superlattice-induced insulating states and valley-protected orbits in twisted bilayer graphene. *Phys. Rev. Lett.* 117, 116804 (2016).
- Kim, K. et al. van der Waals heterostructures with high accuracy rotational alignment. Nano Lett. 16, 1989–1995 (2016).
- Efros, A. L. Coulomb gap in disordered systems. J. Phys. C 9, 2021–2030 (1976).
- Liu, X. et al. Tuning electron correlation in magic-angle twisted bilayer graphene using Coulomb screening. Science 371, 1261–1265 (2021).
- Zhang, Y.-H., Po, H. C. & Senthil, T. Landau level degeneracy in twisted bilayer graphene: role of symmetry breaking. *Phys. Rev. B* 100, 125104 (2019).
- 44. Lian, B. et al. Twisted bilayer graphene. IV. Exact insulator ground states and phase diagram. *Phys. Rev. B* **103**, 205414 (2021).

## Acknowledgements

We acknowledge discussions with A. Hamo and B. Lian. This work was primarily supported by the US Department of Energy, Basic Energy Sciences Office, Division of Materials Sciences and Engineering, under award no. DE-SC0001819, and the Gordon and Betty Moore Foundation through grant GBMF9468 to A.Y. Fabrication of samples was supported by the US Department of Energy, Basic Energy Sciences Office, Division of Materials Sciences and Engineering, under award no. DE-SC0019300. Assistance with the transport measurements and data analysis were provided by the National Science Foundation (DMR-1809802) and the STC Center for Integrated Quantum Materials (NSF grant no. DMR-1231319) (Y.C.). P.J.-H. acknowledges support from the Gordon and Betty Moore Foundation's EPiQS Initiative through grant no. GBMF9463. A.T.P. acknowledges support from the Department of Defense through the National Defense Science and Engineering Graduate Fellowship (NDSEG) Program. Y.X. and S.C. acknowledge partial support from the Harvard Quantum Initiative in Science and Engineering, A.T.P., Y.X. and A.Y. acknowledge support from the Harvard Quantum Initiative Seed Fund. A.V. was supported by a Simons Investigator award and by the Simons Collaboration on Ultra-Quantum Matter, which is a grant from the Simons Foundation (651440). E.K. was supported by a Simons Investigator Fellowship, by NSF-DMR 1411343, and by the German National Academy of Sciences Leopoldina through grant no. LPDS 2018-02 Leopoldina fellowship. P.R.F. acknowledges support from the National Science Foundation Graduate Research Fellowship under grant no. DGE 1745303. This research is funded in part by the Gordon and Betty Moore Foundation's EPiQS Initiative, grant no. GBMF8683, to D.E.P. K.W. and T.T. acknowledge support from the Elemental Strategy Initiative conducted by the MEXT, Japan, via grant no. JPMXP0112101001; JSPS KAKENHI grant no. JP20H00354; and CREST (JPMJCR15F3), JST. This work was performed, in part, at the Center for Nanoscale Systems (CNS), a member of the National Nanotechnology Infrastructure Network, which is supported by the NSF under award no. ECS-0335765. CNS is part of Harvard University.

## **Author contributions**

A.T.P., Y.X., J.M.P., P.J.-H. and A.Y. designed the experiment. A.T.P. and Y.X. performed the scanning SET experiment and temperature-dependent transport measurements, and analysed the data with input from A.Y. S.H.L., A.T.P. and Y.X. performed the transport measurements in the dilution refrigerator. J.M.P., Y.C. and P.J.-H. designed and provided the samples and contributed to the analysis of the results. J.M.P. and Y.X. carried out the simulation of compressibility. E.K., D.E.P. and A.V. performed the theoretical analysis. K.W. and T.T. provided the hBN crystals. All the authors participated in discussions and in writing of the manuscript.

## **Competing interests**

The authors declare no competing interests.

# **Additional information**

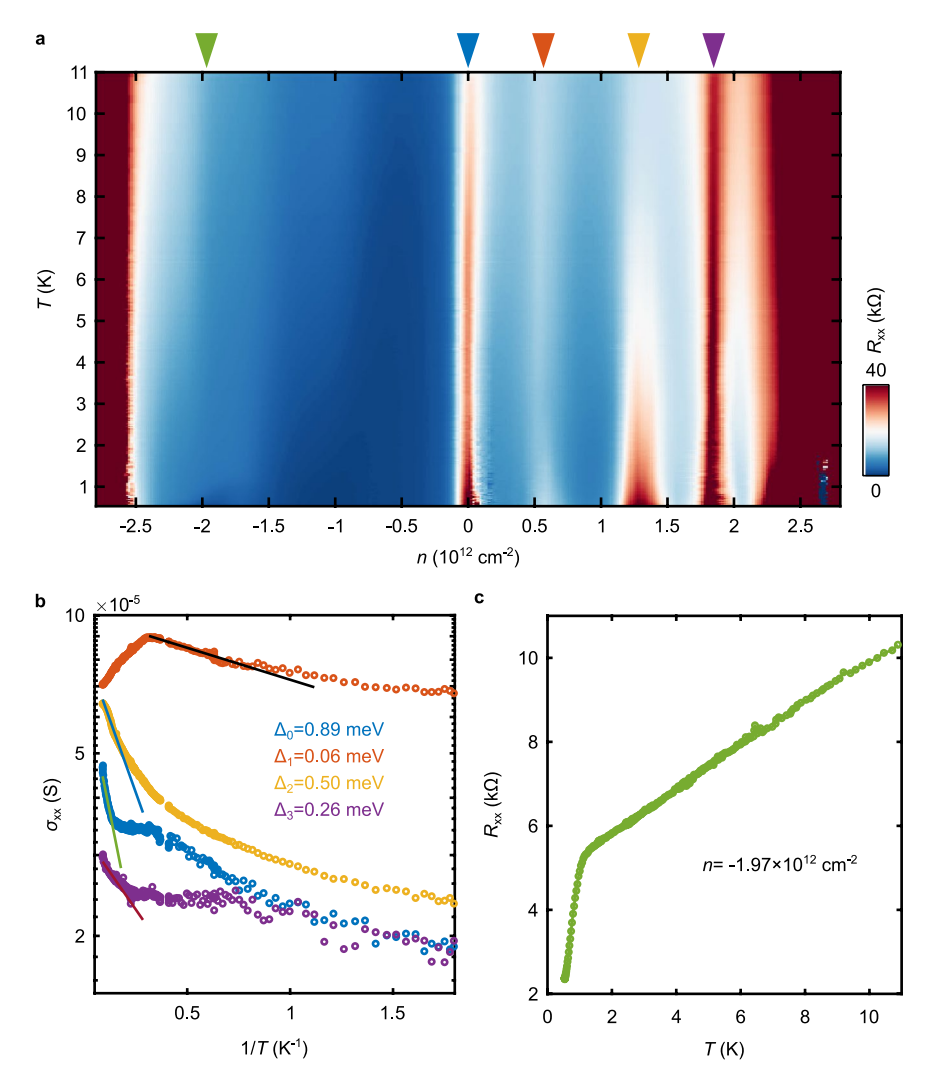
Extended data is available for this paper at https://doi.org/10.1038/s41567-021-01347-4

Supplementary information The online version contains supplementary material available at https://doi.org/10.1038/s41567-021-01347-4.

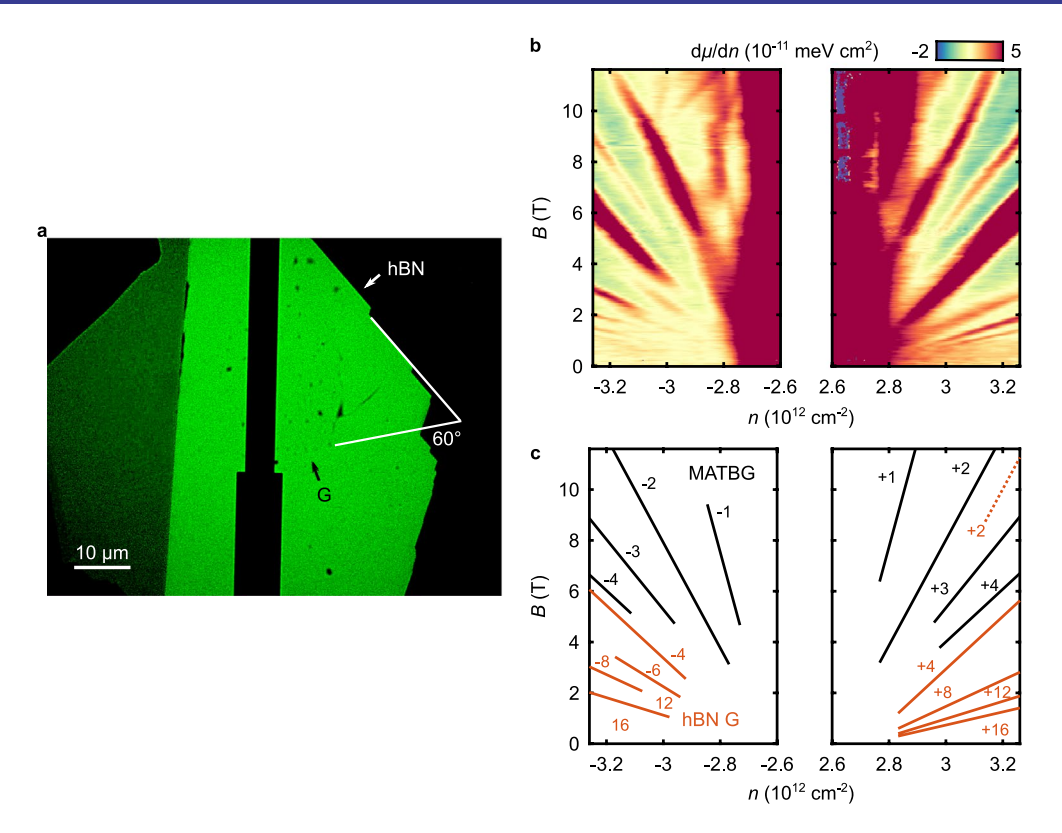
Correspondence and requests for materials should be addressed to Yonglong Xie, Pablo Jarillo-Herrero or Amir Yacoby.

**Peer review information** *Nature Physics* thanks Allan MacDonald and the other, anonymous, reviewer(s) for their contribution to the peer review of this work.

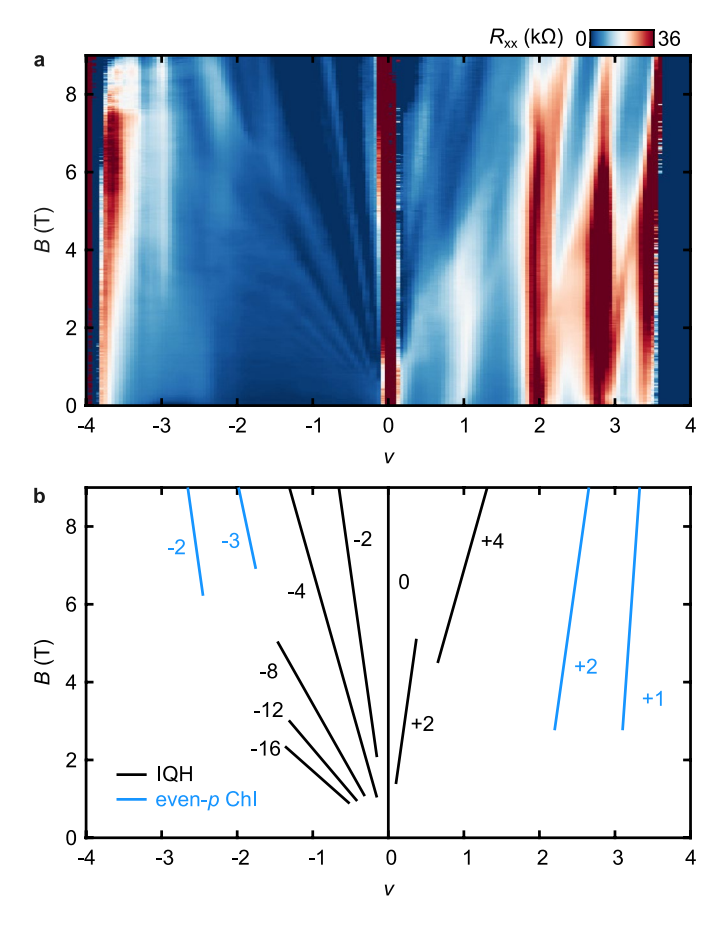
 $\textbf{Reprints and permissions information} \ is \ available \ at \ www.nature.com/reprints.$ 



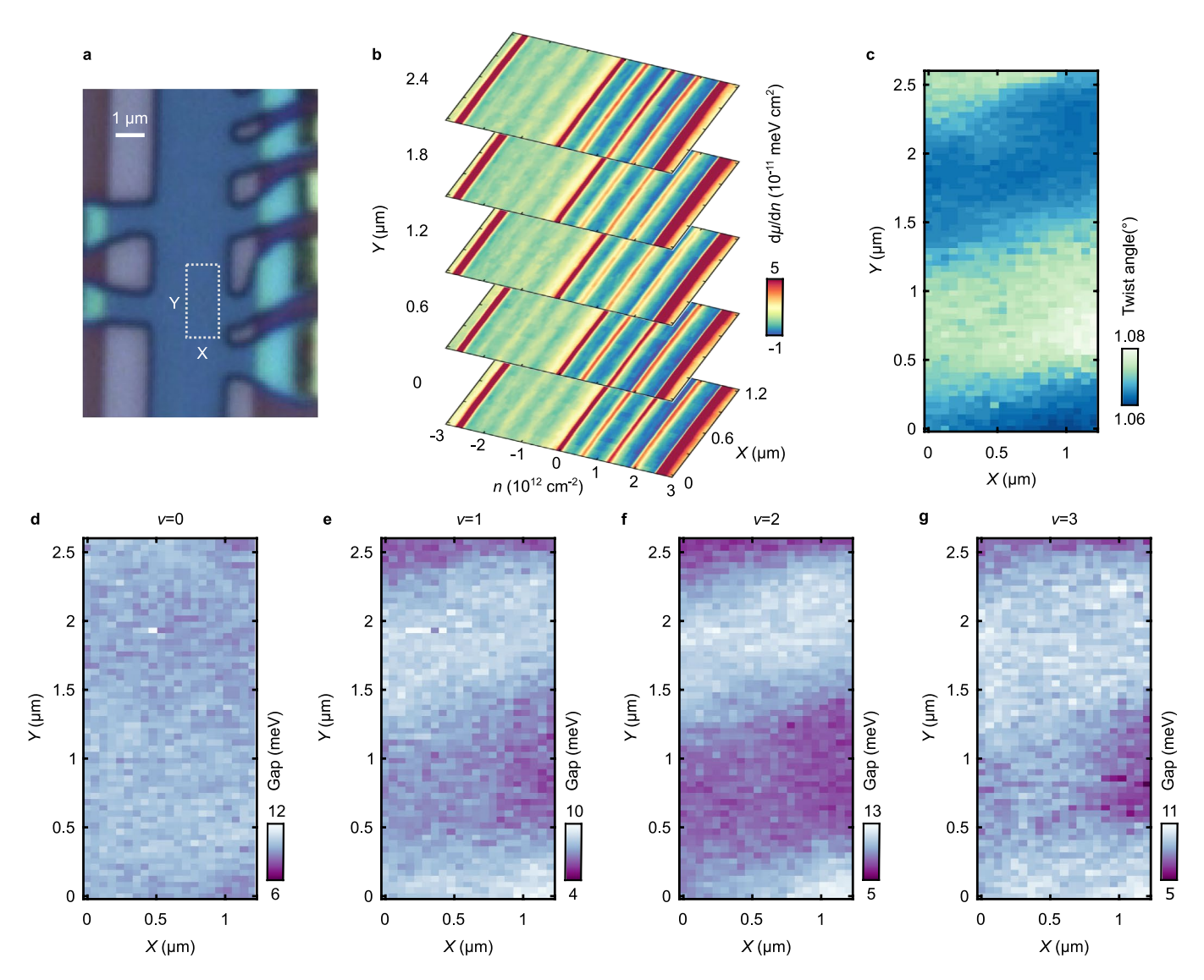
**Extended Data Fig. 1 | Temperature dependent longitudinal resistance. a**,  $R_{xx}$  as a function of carrier density n and temperature from 0.53 K to 11 K. **b**, Semi-log plot of conductance  $\sigma_{xx}$  as a function of inverse temperature at carrier densities indicated by the colored triangles in **a**. The straight lines are fits to  $\sigma_{xx} \propto \exp(-\frac{2\Delta}{k_BT})$  for temperature activated behavior. **c**,  $R_{xx}$  as a function temperature at  $n = -1.97 \times 10^{12}$  cm<sup>-2</sup> showing a superconducting-like transition.



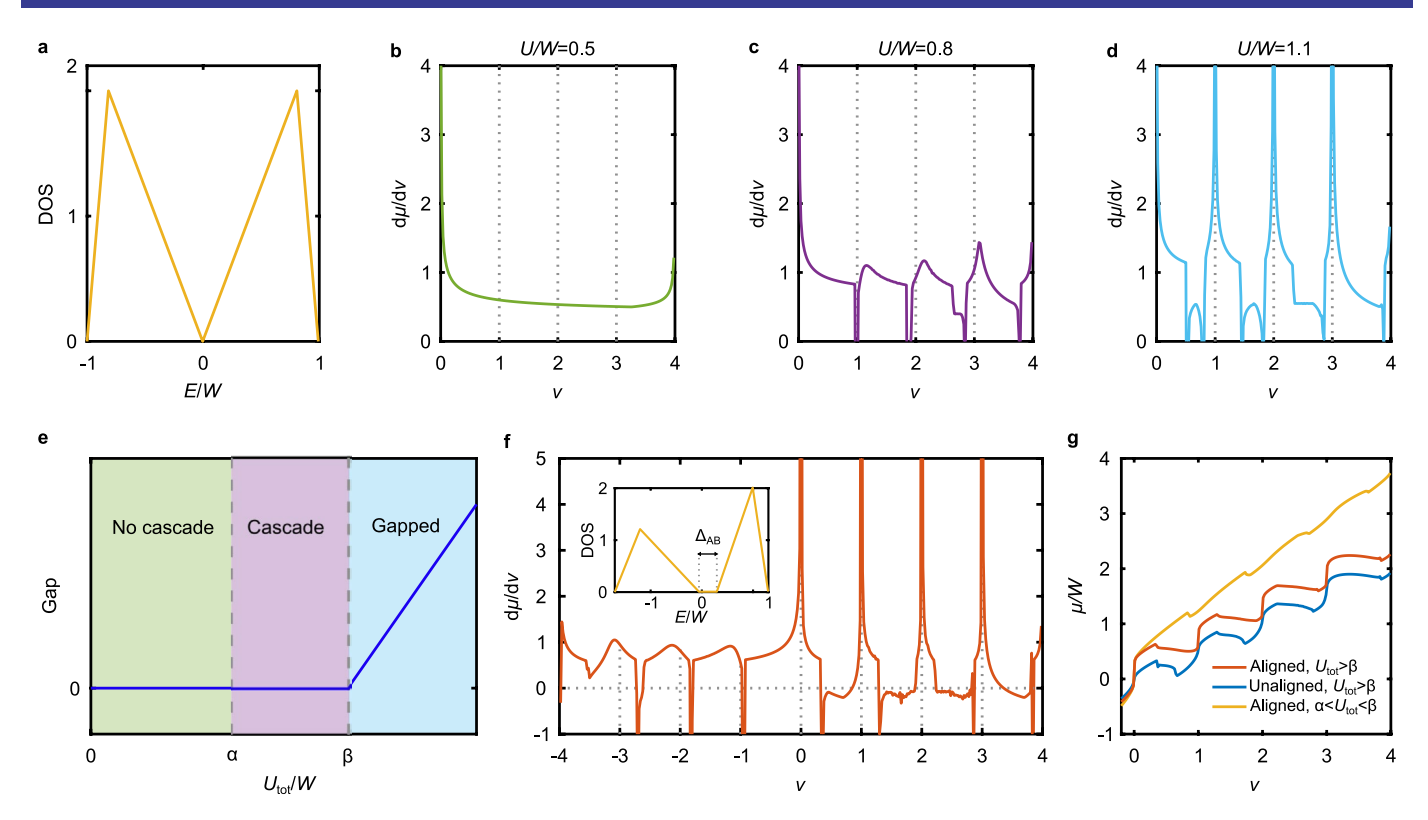
**Extended Data Fig. 2 | Evidence for alignment between hBN and MATBG. a**, Optical image of the stack before etching. The arrows labeled 'hBN' and 'G' indicate the crystallographic edges of the bottom graphene and the bottom hBN, which are aligned with a 60° angular offset. **b**, Inverse compressibility measurements beyond  $v=\pm 4$ , showing a series of incompressible states. **c**, Wannier diagram depicting the incompressible states in **b**. Black and orange lines correspond to states arising from the superlattices formed by MATBG and by the possible alignment between hBN and graphene.



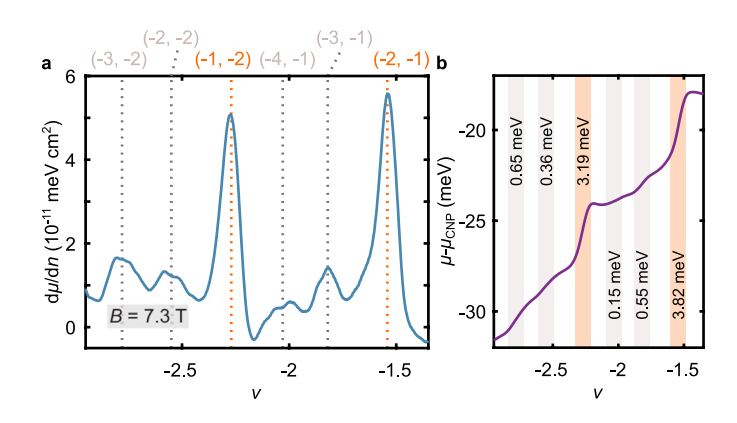
**Extended Data Fig. 3 | Transport Landau fan diagram of MATBG. a**,  $R_{xx}$  as a function of  $\nu$  and B at 10 mK. **b**, Schematic of the Landau level (black) and Chern insulators with even parity (blue) observed in **a**.



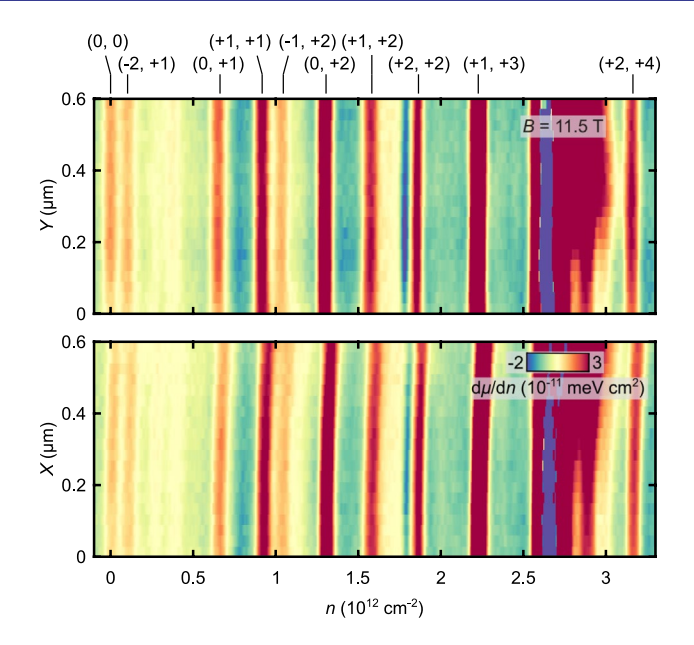
**Extended Data Fig. 4 | Spatially-resolved compressibility measurements at** B = 0 **T. a**, Optical image of the MATBG device. X and Y define the coordinate axis. **b**, Inverse compressibility measurements as a function of carrier density and distance along X at selected Y positions within the white rectangle outlined in **a**, showing the ubiquity of the incompressible states at  $\nu = 0, 1, 2, 3$ . **c**, Local twist angle between the two graphene sheets measured over the region defined by the white rectangle outlined in **a**. **d-g**, Local magnitude of thermodynamic gaps at  $\nu = 0, 1, 2, 3$  over the region defined by the white rectangle outlined in **a**, showing correlation between the gaps at  $\nu = 1, 2, 3$  and the twist angle.



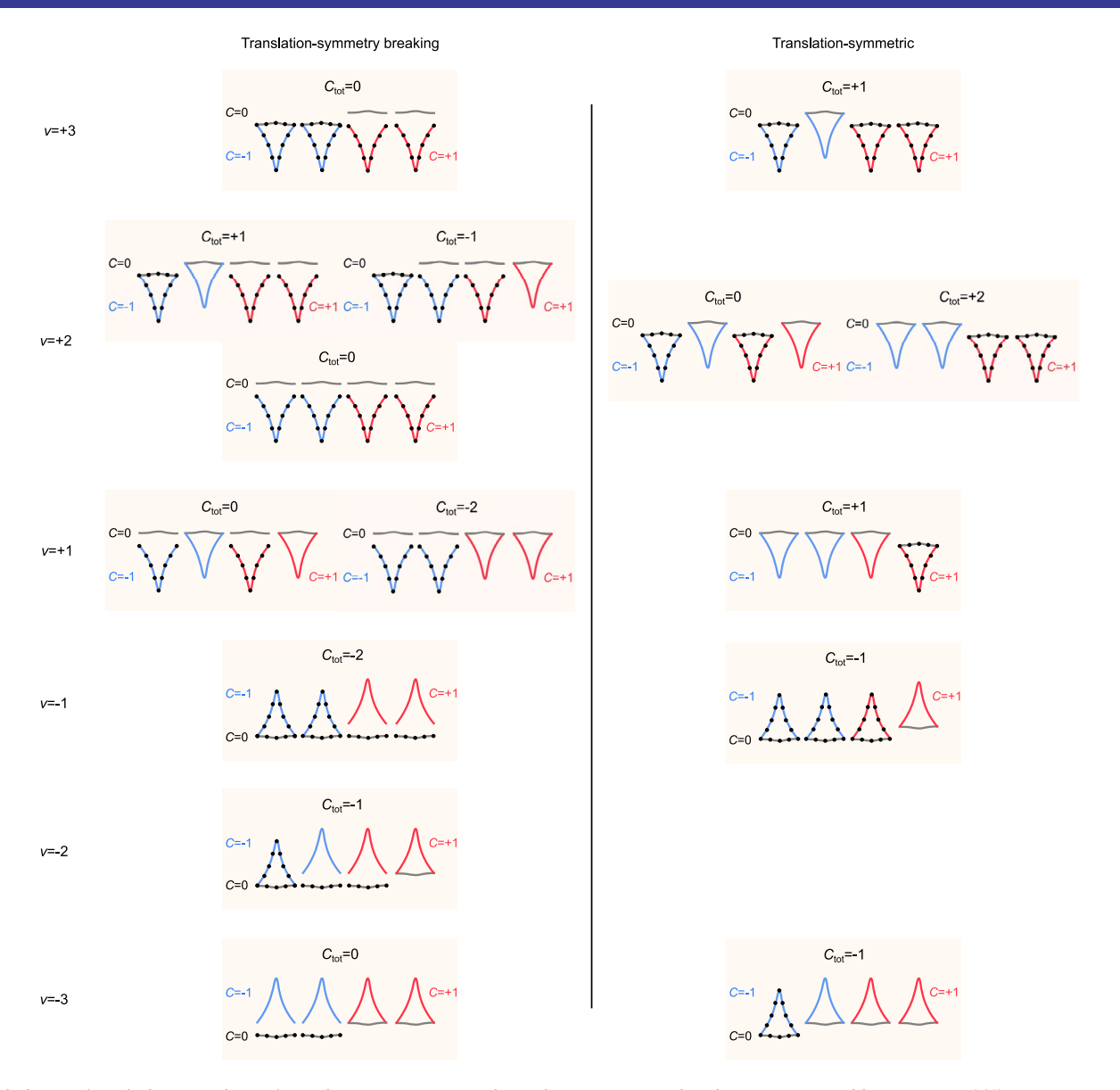
**Extended Data Fig. 5 | Mean-field simulation of inverse compressibility. a**, Simplified symmetric triangular density of states (DOS) of the flat bands in MATBG used for the mean-field calculations in **b**, **c** and **d**. **b-d**, Local inverse compressibility  $d\mu/dn$  calculated using a mean-field model (see Methods) for J=0 and U/W=0.5 (**a**), 0.8 (**b**), and 1.1 (**c**), corresponding to three distinct regimes as shown in **e**. **e**, Schematic illustration of the evolution of the gap at integer fillings as a function of  $U_{tot}/W$  (here  $U_{tot}=U+2J$ ), showing three distinct regimes separated by two critical values  $\alpha$  and  $\beta$ . **f**, Local inverse compressibility  $d\mu/dn$  calculated using the DOS shown in the inset with U=0.55, J=0.35. The bandwidths of the upper and lower flat bands are 1 and 1.65 and the two bands are separated by an asymmetric sublattice gap  $\Delta_{AB}=0.35$ . Our calculation captures the salient features of the measured inverse compressibility in our experiment (Fig. 1e), including the negative compressibility between positive integer fillings. **g**, Chemical potential  $\mu$  relative to its value at the CNP as a function of filling factor  $\nu$ , calculated using the same DOS in the inset to **f**, with different value of interaction strength and sublattice gap. The parameters used for each case are U=0.55, J=0.35,  $\Delta_{AB}=0.35$  for the orange curve, U=0.55, J=0.35,  $\Delta_{AB}=0$  for the blue curve, and U=0.8, J=0,  $\Delta_{AB}=0$  for the yellow curve. We find that interactions are key to the emergence of the gaps at integer fillings, and the presence of a gap at the CNP enhances the values of the gaps if the interaction is strong enough.



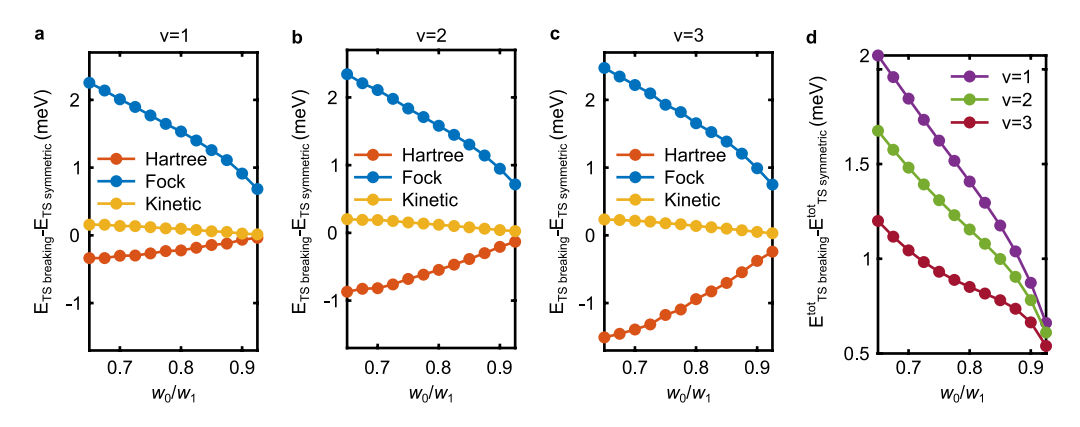
**Extended Data Fig. 6 | Inverse compressibility and chemical potential at 7.3 T. a**,  $d\mu/dn$  as a function of moiré band filling factor  $\nu$ , showing that the incompressible peaks associated with Chern insulators (orange dotted lines) are substantially larger than those of Landau levels (grey dotted lines). **b**, Chemical potential  $\mu$  relative to its value at the CNP as a function of moiré band filling factor  $\nu$ , showing that the energy gaps associated with Chern insulators (orange shaded regions) are substantially larger than those of Landau levels (grey shaded regions).



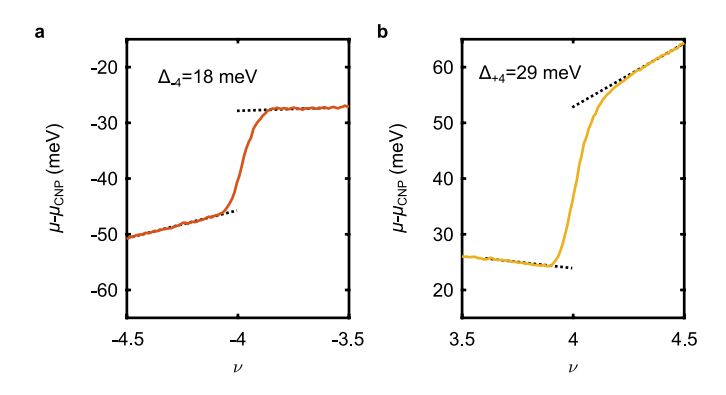
**Extended Data Fig. 7 | Spatial dependence of the incompressible states.** Inverse compressibility measurements for electron doping at  $B = 11.5 \, \text{T}$  over 0.6  $\mu$ m along the X and Y directions (see white dotted rectangle in Extended Data Fig. 4a). The states are labeled by ordered pairs (C, s), which denote the associated Chern number C and the moiré band filling s.



**Extended Data Fig. 8 | Chern numbers of translation-symmetric and translation symmetry breaking incompressible states.** Band filling sequence within the unit cell-doubling model that produces all the experimentally-observed Chern insulators.



**Extended Data Fig. 9 | Hartree-Fock energetics. a-c**, Different contributions to the energy difference between TS-broken and TS-symmetric states as a function of  $w_0/w_1$  at  $\nu=+1$  (**a**), +2 (**b**), +3 (**c**). While the Fock and the kinetic energy remain nearly unchanged, the Hartree energy increases with  $\nu$ , in accordance with the expectation of  $\nu V_H$  (see Methods). **d**, The total energy difference as a function of  $w_0/w_1$  for  $\nu=+1$  (purple),  $\nu=+1$ 



**Extended Data Fig. 10 | Thermodynamic gaps at full fillings. a, b,** Chemical potential relative to the CNP near  $\nu = -4$  (a) and +4 (b), showing the magnitude of the energy gaps separating the flat bands and the remote bands.